Article

Nuclear-Cytoplasmic Shuttling of the Usher Syndrome 1G Protein SANS Differs from Its Paralogue ANKS4B

Jacques S. Fritze , Felizitas F. Stiehler , Uwe Wolfrum *

Posted Date: 30 July 2024

doi: 10.20944/preprints202407.2436.v1

Keywords: usher syndrome; USH1G; SANS; ANKS4B; karyopherin; nuclear-cytoplasmic shuttling

 doi:10.20944/preprints202407.2436.v1

Article

Nuclear-Cytoplasmic Shuttling of the Usher Syndrome 1G Protein SANS Differs from Its Paralogue ANKS4B

Jacques S. Fritze, Felizitas F. Stiehler and Uwe Wolfrum *

Institute of Molecular Physiology, Johannes Gutenberg University Mainz, Mainz, Germany
* Correspondence: wolfrum@uni-mainz.de; Tel.: +49 (0) 6131 39 25148

Abstract: The USH1G protein SANS is a small multifunctional scaffold protein. It is involved in several different cellular processes, such as intracellular transport, in the cytoplasm, or splicing of pre-mRNA, in the cell nucleus. Here, we aimed to gain insight into the regulation of the subcellular localization and the nuclear-cytoplasmic shuttling of SANS and its paralogue ANKS4B, not yet reported in the nucleus. We identified karyopherins mediating the nuclear import and export by screening the nuclear interactome of SANS. Sequence analyses predicted *in silico* evolutionarily conserved nuclear localization sequences (NLSs) and nuclear export sequences (NESs) in SANS, but only NESs in ANKS4B, which are suitable for karyopherin binding. Quantifying the nuclear-cytoplasmic localization of wild-type SANS and NLS/NES mutants, we experimentally confirmed *in silico* predicted NLS and NES functioning in the nuclear-cytoplasmic shuttling *in situ* in cells. The comparison of SANS and its paralogue ANKS4B revealed substantial differences in the interaction with the nuclear splicing protein PRPF31 and in their nuclear localization. Finally, our results on pathogenic USH1G/SANS mutants suggest that the loss of NLSs and NESs and thereby the ability to control nuclear-cytoplasmic shuttling is disease-relevant.

Keywords: usher syndrome; USH1G; SANS; ANKS4B; karyopherin; nuclear-cytoplasmic shuttling

1. Introduction

SANS (scaffold protein containing ankyrin repeats and SAM domain) is encoded by the USH1G gene [1]. Pathogenic variants of USH1G lead to the human Usher syndrome (USH), the most common form of combined hereditary deaf-blindness in humans [2,3]. SANS is a small 52 kDa protein, which consists of 461 amino acids. It is composed of three N-terminal ankyrin repeats (ANK1-3), a central domain (CENT), a sterile alpha motif (SAM), and a PDZ binding motif at the C-terminal end (Figure 1A) [1]. Based on its different functional properties the CENT can be further divided into three subdomains, CENTn1, CENTn2, and CENTc [4]. Context-dependent binding of numerous proteins to its different domains characterizes SANS as a potent scaffold protein [5–12]. In auditory hair cells, SANS plays a crucial role in arranging the four other USH type-1 proteins in the mechanosensitive tip-link complex of the stereocilia [13].

In photoreceptor cells of the retina, SANS functions have been associated with ciliogenesis and the intracellular transport of cargoes to their photosensitive outer segment [6–11]. In addition to these cytoplasm-associated processes, SANS has also been found in the nucleus [7,12,14]. In the nucleus, SANS has been recently linked to the control of pre-mRNA splicing and the activation of the spliceosome by interacting with several spliceosomal components [4,12]. However, the question of how the distribution of SANS between the two cellular compartments the cytoplasm and the nucleus is regulated in the cell remained open.

Interestingly, SANS has a paralogue protein in ANKS4B (ankyrin repeat and SAM domain-containing protein 4B) [14]. Both scaffold proteins are composed of the same principal domain structure (Figure 1A); possess high, up to 80% amino acid sequence homology, and share common binding partners, such as the USH1C protein harmonin [5,14–16]. ANKS4B and SANS are both

 doi:10.20944/preprints202407.2436.v1

located at the tips of microvilli, the brush border microvilli of intestinal enterocytes and the stereocilia, highly modified microvilli of inner ear hair cells, respectively [13,17]. However, while both are found in the cytoplasm, ANKS4B has not yet been reported in the nucleus [14,18]. Moreover, the mechanisms underlying this difference in nuclear-cytoplasmic partitioning have yet to be determined and is one of the questions we address here.

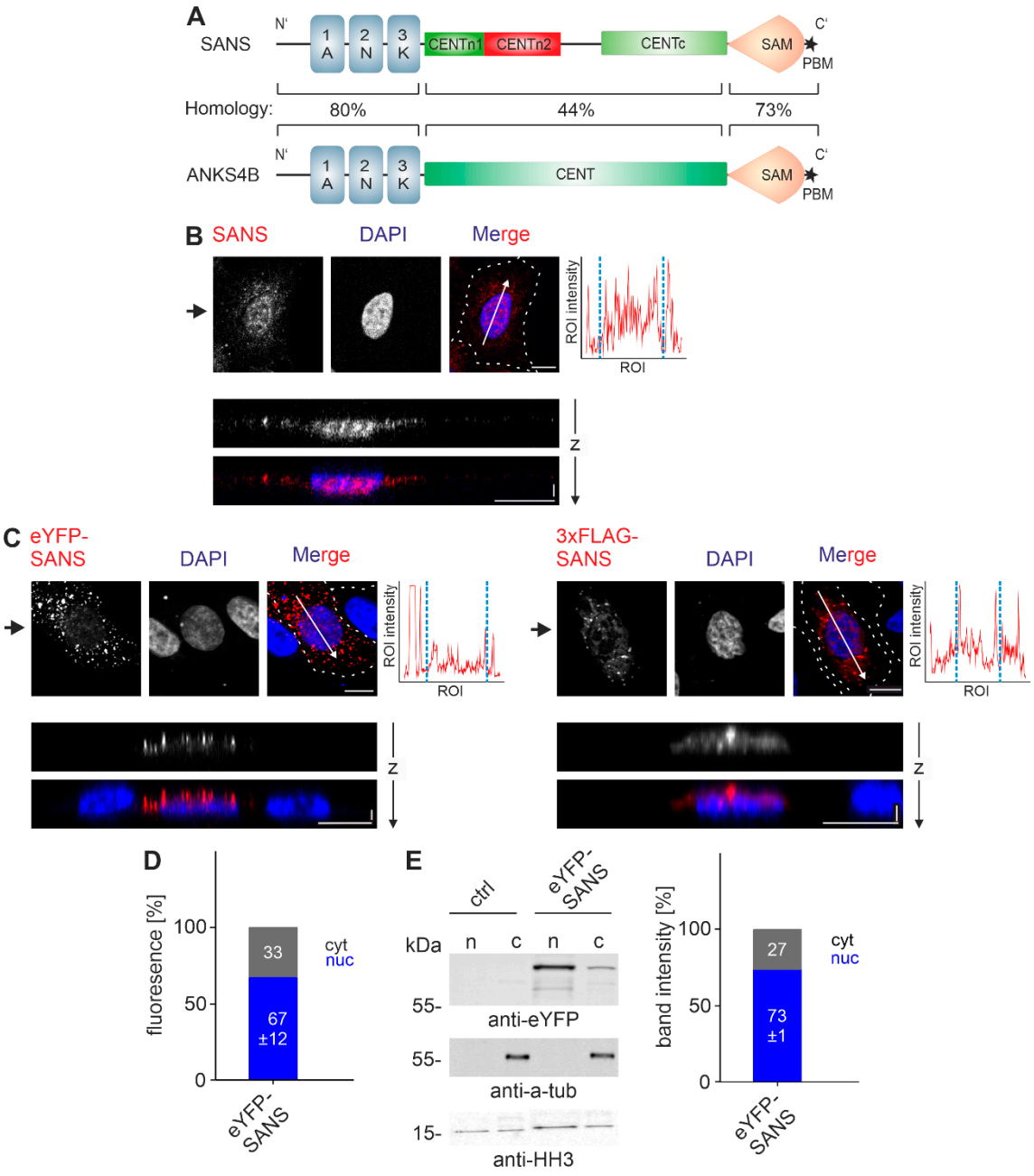

Figure 1. Nuclear localization of SANS. (A) Domain structure of SANS and its paralogue ANKS4B: Both consist of three ankyrin repeats (ANK1-3), a central domain (CENT), divided in SANS into three parts (CENTn1, CENTn2, and CENTc), a sterile alpha motif (SAM), and a C-terminal type-I PDZ binding motif (PBM, asterisk). ANKS4B and SANS amino acid sequences are highly similar in their N- and C-terminal region. **(B, C)** Confocal microscopy of HeLa cells either stained for endogenous SANS **(B)** or transfected with eYFP-SANS, 3xFLAG-SANS **(C)**, counterstained with DAPI. Endogenous SANS and 3xFLAG-SANS was visualized by indirect immunofluorescence of anti-SANS and anti-FLAG. **(B, C)** Endogenous SANS, eYFP-SANS, and 3xFLAG-SANS were localized in the cytoplasm and the nucleus. **(D)** Quantification of eYFP-SANS localization by CellProfiler in HeLa cells. eYFP-SANS is localized in both nucleus and cytoplasm. **(E)** Quantification of eYFP-SANS localization by Cell fractionation assay in HeLa cells. eYFP-SANS is localized similar to (D) in nucleus

 doi:10.20944/preprints202407.2436.v1

and cytoplasm. White arrows in merge images: regions of interests (ROI) of fluorescence intensity plots; blue dashed lines: DAPI positive nuclear extension; black arrows: position of Z-projections. Scale bars: horizontal = 10 μm; vertical = 2 μm. Students t-test was performed for three independent experiments with a minimum of 75 cells.

Nuclear transport is a fundamental cellular process that regulates the localization of macromolecules within the nuclear or cytoplasmic compartments. In humans, approximately 60 proteins participate in nuclear transport, including Ran system proteins that ensure directed and rapid transport, components that form nuclear pore complexes (NPCs) in the nuclear membrane, and karyopherins that transport cargoes through the NPCs [19]. For bidirectional shuttling of nuclear cargo proteins, karyopherins, namely importins and exportins are needed [20]. These bind specifically to linear elements in the nuclear cargos, which are called nuclear localization sequences (NLSs) and nuclear export sequences (NESs), respectively.

In the present study, we aimed to shed light on the nuclear-cytoplasmic shuttling of SANS and its paralogue ANKS4B. We screened the SANS interactome to identify importins and exportins and used *in silico* prediction tools to find conserved NLSs and NESs in SANS protein sequences of several vertebrates. We validated the nuclear-cytoplasmic shuttling potential of wild-type and mutated NLS/NES versions of SANS in HeLa and HEK293T cells by quantifying the nuclear-cytoplasmic localization, which confirmed predicted NLSs and NESs to be important for correct nuclear-cytoplasmic shuttling of SANS. In contrast, strict localization of the SANS paralogue ANKS4B in the cytoplasm is ensured in the absence of any NLS by several NESs. Finally, we provide evidence that the dysregulation and disruption of SANS´ nuclear-cytoplasmic shuttling is relevant for the development of the USH disease in USH1G patients.

2. Materials and Methods

2.1. DNA Constructs

DNA constructs	Reference
eYFP-SANS-S243*	this work
eYFP-SANS-K213E	this work
eYFP-SANS-R447W	this work
eYFP-SANS-L195E	this work
eYFP-SANS-L249E	this work
eYFP-ANKS4B	this work
harmonin-mCherry	this work
eYFP-SANS	[4]
eYFP-SANS-S278Pfs*71	[4]
eYFP-SANS-V132Gfs*3	[4]
eCFP-PRPF31	[4]
harmonin-eCFP	[4]
eCFP-c-eYFP (FRET positive control)	[4]
mRFP-PRPF31	[4]
FLAG-SANS	[12]
pDONR-SANS	[10]
pDONR-SANS-S243*	[10]
pDest-743 (eYFP control)	kindly provided by Ronald Roepman
pDONR-ANKS4B	kindly provided by Katja Luck [21]

 doi:10.20944/preprints202407.2436.v1

2.2. PCR Primers

Primer name	Sequence 5′-3′
K213E_fwd	GGCGAGACCAAGATGCAG
K231E_rev	CCTGGCCGTGCCGTG
R447W_fwd	CGGTGGCAGGCGATG
R447W_rev	CCTCCTCACGGCCC
L195E_fwd	GCGGAGGGCAGCC
L195E_rev	CAGATGCTGCAGCCGG
L249E_fwd	CAGGAGGGCAGCGAC
L249E_rev	CAGGCCCGAGAGCG
qPCR PRPF31 F	CAGACACAGGTAAACGAGGC
qPCR PRPF31 R	CTGGAGTGGGGTGAAGGC

2.3. Antibodies

Antibody name	Supplier	Catalog No.
Rabbit-anti-SANS	Proteintech, Planegg-Martinsried, Germany	21936-1-AP
Rabbit-anti-HistonH3	Cell Signaling Technology, MA, USA	4499
Mouse-anti-α-Tubulin	Merck, Darmstadt, Germany	T9026
Mouse-anti-FLAG	Merck, Darmstadt, Germany	F1804
Mouse-anti-GFP (cross-reaction to eYFP)	Proteintech, Planegg-Martinsried, Germany	66002-1-Ig
Donkey-anti-rabbit Alexa488	ThermoFisher, MA, USA	A-21206
Donkey-anti-rabbit Alexa680	ThermoFisher, MA, USA	A-10043
Donkey-anti-mouse Alexa800	ThermoFisher, MA, USA	SA5-10172

2.4. Cloning

NLS/NES mutants were created by Q5® Site-Directed Mutagenesis Kit according to the manufacturers protocol (NEB, Frankfurt am Main, #E0554S) with pDONR-SANS as a template. pDONR-ANKS4B was kindly provided by Katja Luck [21]. Gateway™ LR reaction into the appropriate destination vector was performed according to the manufacturers protocol (ThermoFisher, Massachusetts, #11791020).

2.5. Cell Lines and Culture

Dulbecco's modified Eagle's medium (DMEM) (ThermoFisher, Massachusetts, #31966021) containing 10% heat-inactivated fetal calf serum (FCS) (Cytiva, 489 #SV30160.03, Freiburg) was used to culture HeLa (kindly provided by AG Doorman, IMP) and HEK293T cells (ATCC: CRL-3216).

2.5. Immunocytochemistry

Cells were fixed with 4% paraformaldehyde in PBS for 10 min at RT, washed with PBS, permeabilized with PBST (0.1% Triton-X100 (Roth, Karlsruhe, # 3051.1)) 5 min at RT and blocked with 0.1% ovalbumin, 0.5% fish gelatine in PBS for 1 h at RT. Primary antibodies were incubated overnight at 4 °C, followed by washing with PBS and secondary antibody in a blocking solution containing DAPI (1 mg/mL) (Roth, Karlsruhe, #6335.1) incubations 1 h at RT. After washing, cells were mounted in Mowiol (Roth, Karlsruhe, #0713.2).

 doi:10.20944/preprints202407.2436.v1

2.6. Fluorescence (co-)Localization Observation

Cells were seeded in 6 well plates with a density of 250.000 cells/well. Cells were transfected with Lipofectamine™ LTX as described by the manufacturer (ThermoFisher, Massachusetts, #15338100) and incubated for 24 h. If indicated cells were treated with 5 nM Leptomycin-B (Selleck Chemicals GmbH, Munich, #S7580) or 40 µM Importazole (Merck, Darmstadt, #401105) for 4h before fixation. If indicated cells were treated with Lipofectamine™ RNAiMAX for 24 h as described by the manufacturer (ThermoFisher, Massachusetts, #13778075). siRNA for PRPF31 (IDT, Leuven, #TriFECTa®Kit DsiRNA Duplex, 5'-AGCUAUGGGAUAGUAAGAUGUUUGC-3') was used. Knockdown efficiency was validated by qPCR as described previously [12]. Cells were fixed with 4% paraformaldehyde in PBS for 10 min at RT and counterstained for 10 min in DAPI (1 mg/mL) (Roth, Karlsruhe, #6335.1). After washing, cells were mounted in Mowiol (Roth, Karlsruhe, #0713.2).

2.7. Fluorescence Microscopy

Fixed cells were observed with a Leica TCS SP5 or Zeiss LSM900. Images were analyzed with Fiji [22] (https://imagej.net/software/fiji/downloads). Intensity plot was performed over the indicated region of interest with the Fiji Plugin Plot Profile. Z-projections were performed over the indicated region of interest with the Fiji Plugin Orthogonal Views. Pearson coefficient was performed with the Fiji Plugin Coloc 2.

2.8. In Silico Prediction

The amino acid sequence of the protein of interest was used from uniprot. The following sequences were used: *Homo sapiens* SANS (Q495M9); *Macaca nemestrina* SANS (A0A2K6BVI9); *Mus musculus* SANS (Q80T11); *Danio rerio* SANS (A0A8M1RQW2); *Xenopus laevis* SANS (A0A8J0TLE4); *H. sapiens* ANKS4B (Q8N8V4). NLSs were predicted with a given amino acid sequence by NLStradamus [23]. NESs were predicted with a given amino acid sequence by LocNES [24]. Homology of SANS NLS/NES was aligned with Blastp (https://blast.ncbi.nlm.nih.gov/Blast.cgi?PAGE =Proteins, accessed on 02nd April 2024). Homology of SANS and ANKS4B was calculated from the alignment of Blastp (https://blast.ncbi.nlm.nih.gov/Blast.cgi?PAGE =Proteins, accessed on 01st March 2024).

2.9. CellProfiler Based Nuclear/Cytoplasmic Ratio Quantification

Images were preanalyzed with Fiji and then analyzed automatically with CellProfiler [25]. For analysis, we used the pipeline "Human cells" (https://cellprofiler-examples.s3.amazonaws.com/ExampleHuman.zip) with adjustments available on Github: https://github.com/LabWolfrum/Fritze_et_al_2024_SANS_Nuclear_localization

In short, three tif files (protein of interest, DAPI, Brightfield) were used as input. Primary and secondary structures were identified with CellProfiler and the mean intensity of the eYFP channel of the nucleus and cytoplasm was used for further statistical analysis.

2.10. CellFractionation Assay

Cells were seeded in 6 well plates with a density of 250.000 cells/well. Cells were transfected with Lipofectamine™ LTX as described by the manufacturer (ThermoFisher, Massachusetts, #15338100) and incubated for 24h. Cells were harvested and lysed into nuclear and cytoplasmic fractions with the commercial kit NE-PER™ (ThermoFisher, Massachusetts, #78833). Protein amount was measured with a BCA assay, and proteins were eluted with 5x Laemmli buffer, separated by SDS-PAGE followed by total protein measurement (Revert™ 700 Total Protein Staining) (LICOR, Nebraska, 926-11010) and Western blotting. Relative intensity was calculated with Fiji for the GFP (cross-reaction for eYFP) band and normalized to total protein and HistoneH3 band.

 doi:10.20944/preprints202407.2436.v1

2.11. Fluorescence Resonance Energy Transfer (FRET) Acceptor Photobleaching Assay

HeLa cells were seeded in 6 well plates with a density of 250.000 cells/well. Cells were transfected with Lipofectamine™ LTX as described by the manufacturer (ThermoFisher, Massachusetts, #15338100). Fixed HeLa cells were analyzed with a Leica TCS SP8 and FRET acceptor photobleaching was performed following the Leica protocol (https://downloads.leica-microsystems.com/TCS%20SP8/Application%20Note/FRET_AB_with%20SP8-AppLetter_EN.pdf). eCFP was used as donor (D) and eYFP as acceptor (A). The acceptor was bleached at 100% laser intensity for 10 repeats. FRET efficiency was calculated via: $\mathrm{FRET_{eff}} = \left(\frac{(\mathrm{D_{post}} - \mathrm{D_{pre}})}{\mathrm{D_{post}}}\right)$. To exclude cellular structure the mean of six regions of interest (ROI) in the bleached area was calculated and the FRET efficiency of an unbleached region (≥ 3 µm away from bleached ROI) was subtracted from the mean. Bleach efficiency was calculated via the formula $\mathrm{Bleach_{eff}} = \left(\frac{1-\mathrm{A\_post}}{\mathrm{A\_pre}}\right) * 100$. Only ROIs with > 60% bleach efficiency were used for analysis. Data was normalized to 1 by the positive control eCFP-c-eYFP.

2.12. SANS Nuclear Interactome Analysis

SANS nuclear interactome analysis in HEK293T cells [12] were used as input for the Cytoscape plugin ClueGO according to their gene names based on HGNC. Gene Ontology (GO) term enrichment analysis was performed by ClueGO v2.3.3.

2.13. Statistics

Statistical analysis was performed with R-Studio [26]. The statistical methods are listed in corresponding individual legends. Results are shown from at least 3 separate experiments. Significance was determined as: *p≤0.05, **p≤0.009, ***p. ≤0.0009.

3. Results

3.1. Subcellular Localization of SANS

Recent work indicated that SANS shuttles from the cytoplasm into the nucleus [7,12,14]. We confirmed cytoplasmic and nuclear localization of endogenous SANS in HeLa cells by immunocytochemistry using anti-SANS antibodies (Figure 1B) and in HeLa cells transfected with eYFP-SANS and 3xFLAG-SANS monitoring eYFP fluorescence or indirect anti-FLAG immunofluorescence, respectively (Figure 1C). Quantification of eYFP-SANS fluorescence in cytoplasmic and nuclear compartments by CellProfiler revealed that approximately 30% of SANS was present in the cytoplasm and 70% in the nucleus in HeLa cells (Figure 1D). Quantitative analysis of the compartmental distribution in eYFP-SANS expressing HEK293T cells confirmed that most SANS (77%) was localized in the nucleus (Figure S1A). Next, we biochemically validated the compartmental distribution of SANS by cytoplasmic-nuclear cell fractionations in eYFP-SANS transfected HeLa cells (Figure 1E). Western blot analysis of the nuclear and cytoplasmic fractions showed that approximately 70% of SANS was present in the nucleus confirming the obtained *in situ* data.

Taken together our experimental data consistently demonstrated that SANS is predominantly localized in the nucleus.

3.2. Identification of Karyopherins in the Nuclear Interactome of SANS

To identify potential karyopherins that bind to SANS, we screened the previously published nuclear interactome of SANS in HEK293T cells [12] for importins and exportins. We identified in the GO-term gene clusters “nuclear import” (GO:0051170) and “nuclear export” (GO:0051168) (Cytoscape plugin ClueGO, https://apps.cytoscape.org/apps/cluego, accessed on 6th of June 2024; Table S1) eight nuclear importins and three exportins including exportin-1/CRM1, the main nuclear protein exporter (Table 1).

 doi:10.20944/preprints202407.2436.v1

Table 1. Nuclear exportins and importins identified as potential SANS interacting proteins in the nucleus [12].

Gene	Protein	Export/Import	NLS/NES recognition
KPNB1	Importin-β	Protein importer	classic NLS [20] non classic NLS [20]
IPO4	Importin-4	Protein importer	classic NLS [27] non classic NLS [20]
IPO5	Importin-5	Protein importer	classic NLS [28] non classic NLS [20]
IPO7	Importin-7	Protein importer	classic NLS [29] non classic NLS [20]
IPO8	Importin-8	Protein importer	classic NLS [29] non classic NLS [20]
IPO9	Importin-9	Protein importer	non classic NLS [20]
IPO11	Importin-11	Protein importer	non classic NLS [20]
IPO13	Importin-13	Protein importer	classic NLS [30] non classic NLS [30]
XPO1	CRM1/Exportin-1	Protein exporter	NES
XPO5	Exportin-5	dsRNA exporter	-
XPOT	Exportin-T	amino-acylated tRNAs export	-

Subsequently, we investigated their role by applying commercially available importin and exportin inhibitors to eYFP-SANS transfected HeLa cells followed by confocal microscopy analysis and quantification with CellProfiler [25]. Applying the importin-β inhibitor Importazole (IPZ) to transfected HeLa had no effect on eYFP-SANS subcellular localization (Figure S2A-B). Further, we investigated the role of the exportin CRM1 in SANS nuclear export by treating eYFP-SANS HeLa cells with the CRM1 inhibitor Leptomycin-B (LMB) [31]. Confocal microscopy and CellProfiler-based quantification of the subcellular localization of SANS revealed that applications of LMB to the cells resulted in a significant increase in the nuclear localization of SANS when compared to the untreated control (Figure 2A,B). In contrast, treatments with the LMB solvent DMSO had no effect on the nuclear localization. Combined, the treatment revealed that the core export of SANS is mediated by CRM1.

Preprints.org (www.preprints.org) | NOT PEER-REVIEWED | Posted: 30 July 2024 doi:10.20944/preprints202407.2436.v1

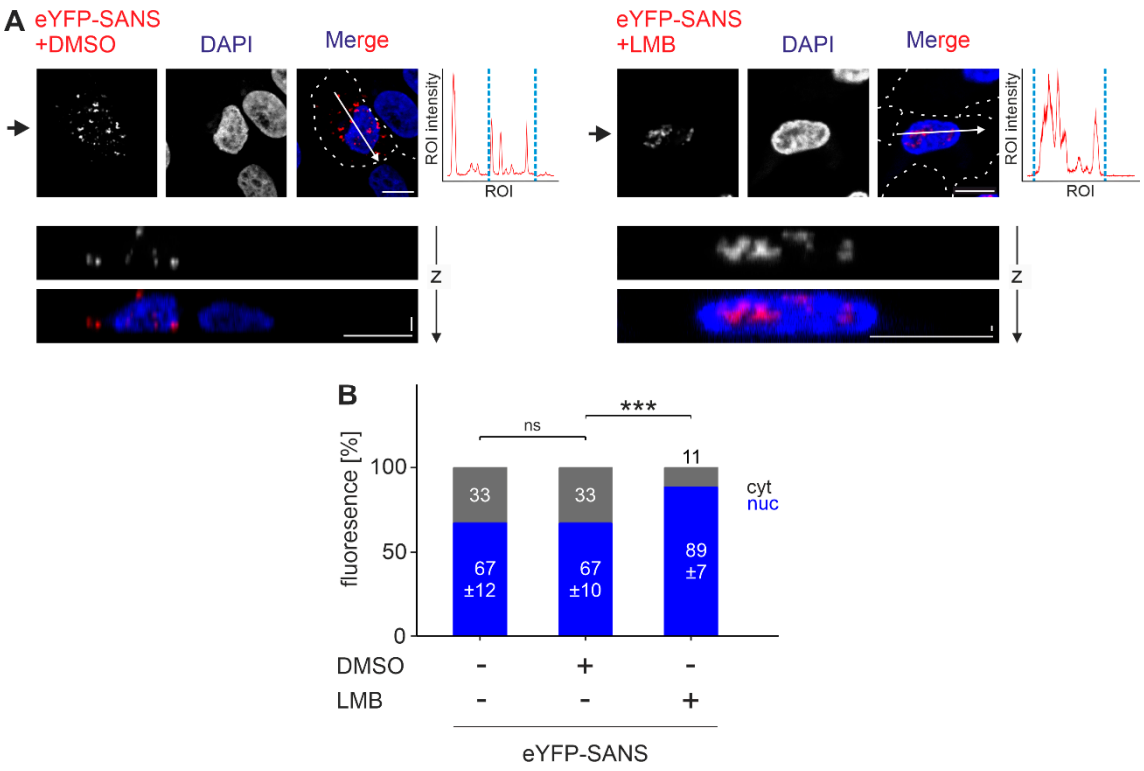

Figure 2. Nuclear localization of SANS in HeLa after treatment with Leptomycin-B. (A) Confocal microscopy of HeLa cells transfected with eYFP-SANS (red) and treated with 5 nM CRM1-inhibitor LeptomycinB (LMB) or its solvent DMSO. **(B)** Quantification of (A) by CellProfiler. eYFP-SANS was significantly enriched in the nucleus after LMB treatment. White arrows in merge images: regions of interests (ROI) of fluorescence intensity plots; blue dashed lines: DAPI positive nuclear extension; black arrows: position of Z-projections. Scale bars: horizontal = 10 µm; vertical = 2 µm. Students t-test was performed for three independent experiments with a minimum of 75 cells.

3.3. In Silico Prediction and Evolutionary Conservation of Nuclear Localization Sequences (NLSs) and Nuclear Export Sequences (NESs) in SANS

For nuclear transport karyopherins bind to nuclear localization sequences (NLSs) and nuclear export sequences (NESs) present in the cargo molecules [20]. To identify NLSs and NESs in the human SANS sequence we used the prediction tools NLStradamus [23] and LocNES [24], respectively (Table 2). In addition, the predicted consensus sequences were scored from 0 to 1.

NLStradamus predicted two NLSs within SANS, located in the CENTn2 (NLS_$1^{213-224}$) and SAM domains (NLS_$2^{436-447}$), with scores of 0.733 and 0.679, respectively, both above the NLS threshold of 0.6 [23] (Figure 3A). LocNES identified three NESs within SANS, two in the CENTn2 domain (NES_$1^{181-195}$ and NES_$2^{235-249}$) and one in the SAM domain (NES_$3^{406-420}$), with scores ranging from 0.250 to 0.462, all above the NES threshold of 0.1 [24] (Figure 3A). In addition, we classified the predicted NESs into distinct classes of NES motifs binding to the exportin CRM1 (Table 2).

Table 2. Nuclear localization (NLSs) and export sequences (NESs) of SANS predicted by LocNES and NLStradamus.

NLS/NES	Sequence	Score	CRM1-class	NLS/NES mutations
NLS_$1^{213-224}$	213-KTKMQKKLERRK-224	0.733	-	K213E: ETKMQKKLERRK
NLS_$2^{436-447}$	436-RKKILGAVRRRR-447	0.679	-	R447W: RKKILGAVRRRW
NES_$1^{181-195}$	181-LTSSTLSRRLQHLAL-195	0.262	1a	L195E: LTSSTLSRRLQHLAE

 doi:10.20944/preprints202407.2436.v1

NES_2$^{235-249}$	235-EDGRKSARSLSGLQL-249	0.250	1b	L249E: EDGRKSARSLSGLQE
NES_3$^{406-420}$	406-ALLRQEKIDLEALML-420	0.462	2	n.a.

Sequence alignments of the identified NLSs and NESs motifs of SANS across five diverse vertebrates from human to frog, namely *H. sapiens*, *M. nemestrina*, *M. musculus*, *D. rerio*, and *X. laevis* revealed high to medium conservation of the motifs (Figure 3B-F). Notably, *D. rerio* and *X. laevis* have two and three Ush1g genes encoding SANS, respectively. However, all sequences of the predicted NLSs and NESs in the multiple genes of the respective species are identical.

Both NLSs are 100% conserved throughout all the three mammals. In NLS_1$^{213-224}$ of *D. rerio* and *X. laevis* we observed exchanges of two positive charged amino acids, namely arginine to lysins. However, in NLS_2$^{436-447}$ of both species, exchanges between charged and uncharged amino acids were found.

The CRM1-consensus motif of NES_3$^{406-420}$ is 100% conserved throughout all vertebrate species tested. In contrast, NES_1$^{181-195}$ was conserved in all vertebrates except for *X. laevis*. NES_2$^{235-249}$ was also conserved in all tested species but differed in its starting residue in *M. musculus*, *D. rerio* and *X. laevis*. Taken together, *in silico* analyses predicted two NLSs and three NES/CRM1 motifs in SANS that differ in their probabilities and evolutionary conservation in vertebrates.

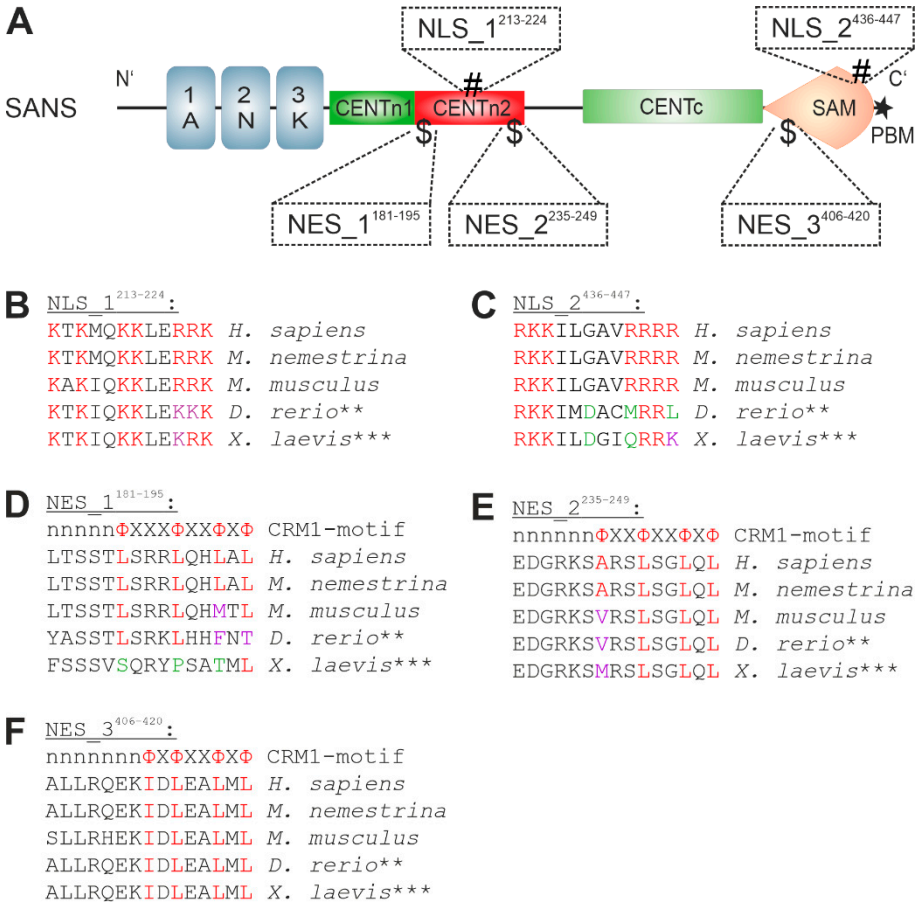

Figure 3. Prediction of nuclear localization sequences (NLSs) and nuclear export sequences (NESs) of SANS. (A) Three NES ($; NES_1$^{181-195}$, NES_2$^{235-249}$, NES_3$^{406-420}$) and two NLS (#; NLS_1$^{213-224}$, NLS_2$^{436-447}$) were predicted for SANS by NLStradamus and LocNES. **(B-F)** Conservation of SANS NLS_1$^{213-224}$ **(B)**, NLS_2$^{436-447}$ **(C)**, NES_1$^{181-195}$ **(D)**, NES_2$^{235-249}$ **(E)** and NES_3$^{406-420}$ **(F)** with blastp to Human SANS for five model organisms. In **B-C**, positive charged residues (red), arginine-to-lysin exchanges (purple), charge changes (green) are indicated in NLSs. In **D-F**, first line: position of consensus amino acids residues in CRM1-motif are indicated in red. Valid (purple) and invalid (green) residue changes in the consensus sequence of the CRM1 motif are indicated. ** and *** indicate

 doi:10.20944/preprints202407.2436.v1

that the genomes of *D. rerio* and *X. laevis* possess two and three *Ush1g* genes encoding for SANS orthologues, respectively, which do not differ at the NLS and NES sequences.

3.4. Analysis of the Nuclear Localization Efficiency of Predicted NLS in SANS in the Cell

Next, we examined the efficiency of the two predicted NLSs of SANS in cells. Using site-specific mutagenesis, we mutated positively charged residues to uncharged or negatively charged residues in the NLSs of human SANS that should prevent karyopherin binding to the mutated NLS (Table 2, Figure 4A). eYFP-tagged wild-type SANS and SANS NLS mutants (SANS^{K213E}/ΔNLS_1$^{213-224}$, SANS^{R447W}/ΔNLS_2$^{436-447}$) were transfected into HeLa cells (Figure 4B) and HEK293T cells (Figures S1A) and the subcellular distribution of the SANS variants was then assessed by confocal microscopy. Confocal images, their z-projections, and fluorescence intensity plots of eYFP-tagged SANS^{K213E} and SANS^{R447W} indicated an increase of SANS in the cytoplasm of HeLa and HEK293T cells. CellProfiler-based quantification of the SANS localization showed a significant decrease in nuclear localization of SANS^{K213E} (ΔNLS_1$^{213-224}$) compared to wild-type SANS in both HeLa and HEK293T cells (Figure 4C, Figures S1B). Analysis of SANS^{R447W} (ΔNLS_2$^{436-447}$) showed a decrease in its nuclear localization that was not significant in HeLa cells but was slightly significant in HEK293T cells (Figure 4C; Figures S1B). In summary, our findings indicate that NLS_1$^{213-224}$ has a stronger role in the nuclear localization of SANS than NLS_2$^{436-447}$.

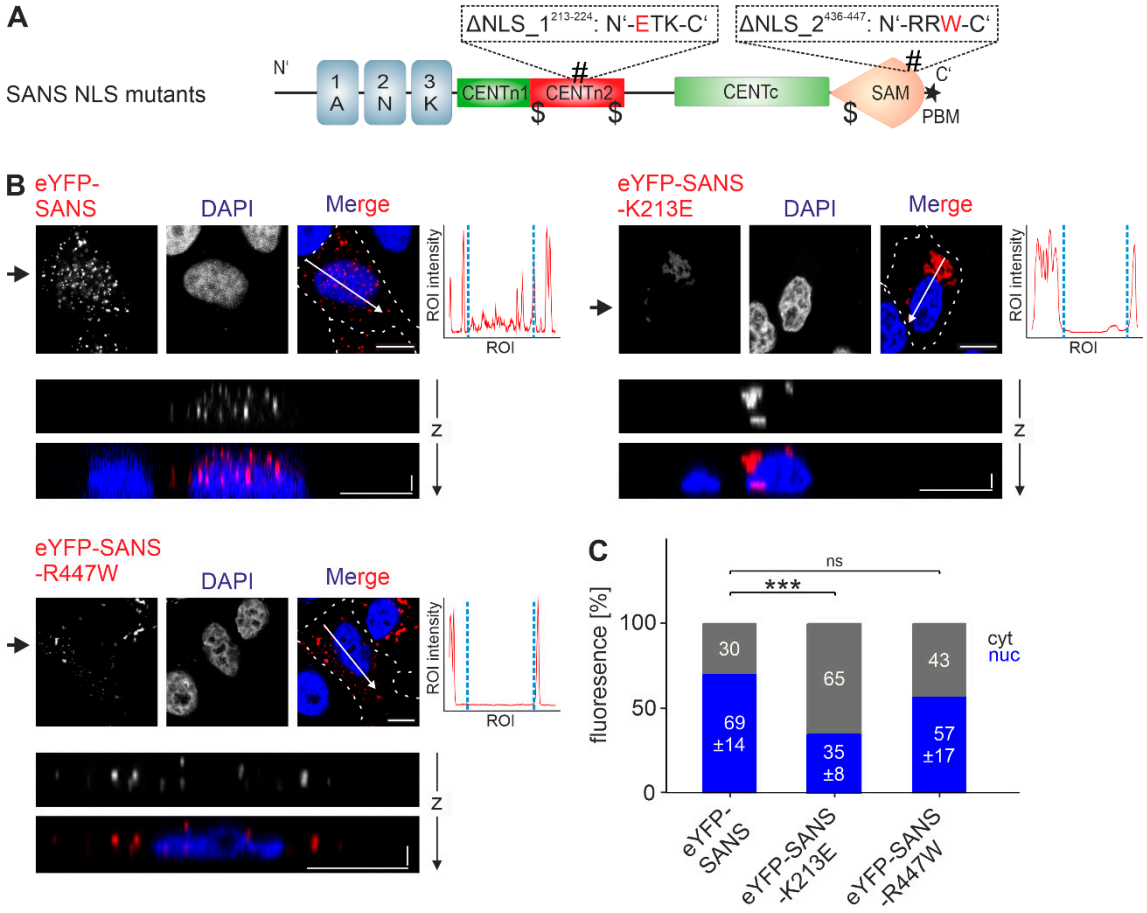

Figure 4. Subcellular localization of SANS NLS mutants. (A) Domain structure of SANS, the two NLS (#) mutants K213E (ΔNLS_1$^{213-224}$) and R447W (ΔNLS_2$^{436-447}$) are indicated above the cartoon. **(B)** Confocal microscopy of HeLa cells transfected with eYFP-SANS (red) or SANS NLS mutants, counterstained with DAPI. **(C)** Quantification of (B) by CellProfiler. eYFP-SANS^{K213E} differed significantly from eYFP-SANS. White arrows in merge images: regions of interests (ROI) of fluorescence intensity plots; blue dashed lines: DAPI positive nuclear extension; black arrows: position of Z-projections. Scale bars: horizontal = 10 µm; vertical = 2 µm. Students t-test was performed for three independent experiments with a minimum of 75 cells.

Preprints.org (www.preprints.org) | NOT PEER-REVIEWED | Posted: 30 July 2024 doi:10.20944/preprints202407.2436.v1

3.5. Analysis of the Nuclear Export Efficiency of Predicted NES in SANS in the Cell

We examined the nuclear export efficiency of the predicted NESs of SANS in the cell. We designed and generated SANS NES mutants by exchanging hydrophobic residue leucine (L) to glutamic acid (E) by site-specific mutagenesis for SANS NES_1$^{181-195}$ and SANS NES_2$^{235-249}$ (Table 2, Figure 5A). This resulted in SANS^{L195E} (ΔNES_1$^{181-195}$) and SANS^{L249E} (ΔNES_2$^{235-249}$), which were no longer predicted as a NES by LocNES. The two NES mutants were tagged with eYFP, transfected into HeLa and HEK293T cells, and examined by confocal microscopy (Figure 5B, Figure S3A). Unexpectedly, eYFP-SANS^{L249E} formed prominent cytoplasmic aggregates, while eYFP-SANS^{L195E} predominantly localized in small nuclear droplets, as shown by fluorescence intensity plotting and z-projection. CellProfiler-based quantifications showed no significant difference in the nuclear-cytoplasmic ratio of eYFP-SANS^{L249E} (ΔNES_2$^{235-249}$) compared with eYFP-SANS (Figure 5C, Figure S3B). In contrast, the quantification for eYFP-SANS^{L195E} (ΔNES_1$^{181-195}$) exhibited a significant increase in the nuclear localization compared to eYFP-SANS. These findings suggest that NES_1$^{181-195}$ but not NES_2$^{235-249}$ plays a role in SANS nuclear export.

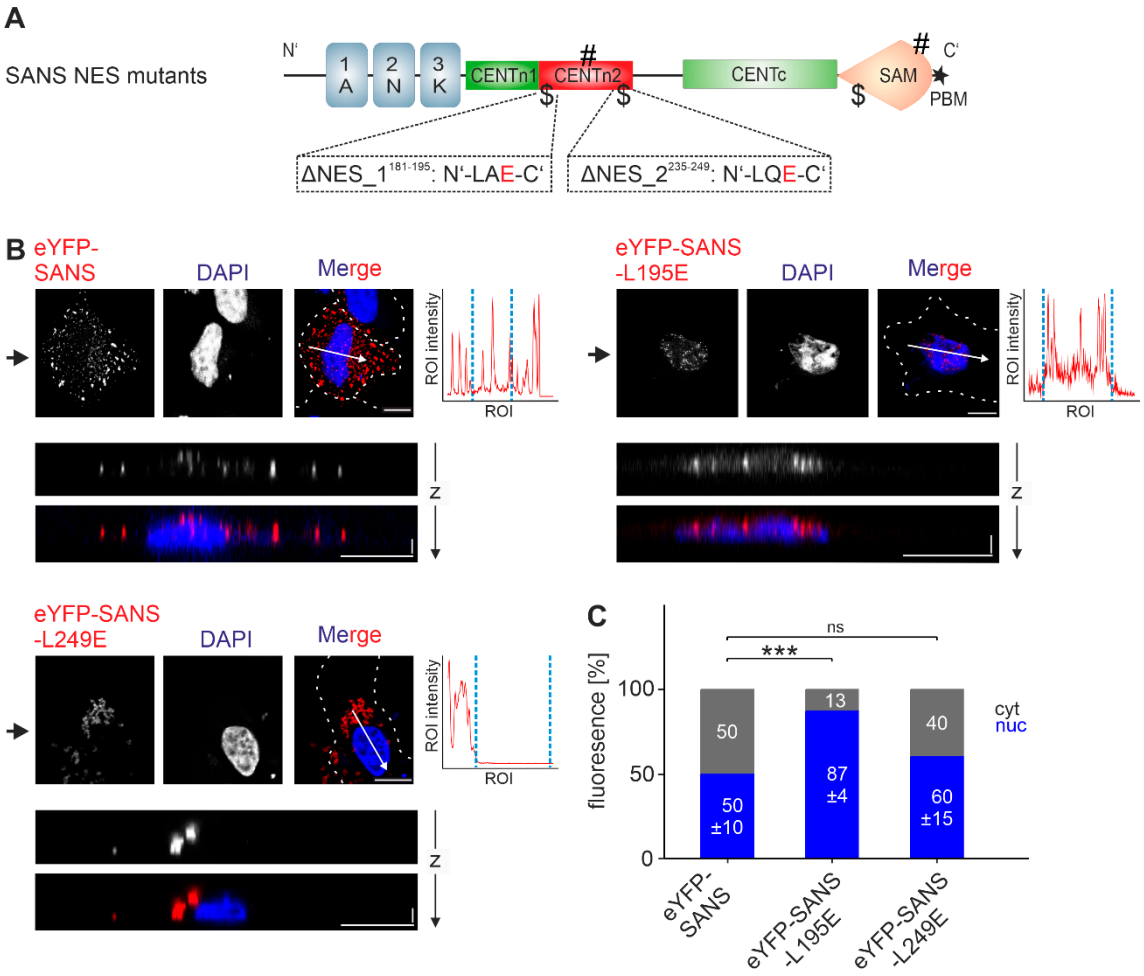

Figure 5. Localization of SANS NES mutants. (A) Domain structure of SANS, the two NES (\$) mutants L195E (ΔNES_1$^{181-195}$) and L249E (ΔNES_2$^{235-249}$) are indicated below the cartoon. **(B)** Confocal microscopy of HeLa cells transfected with eYFP-SANS (red) or NES mutants, counterstained with DAPI. **(C)** Quantification of (B) by CellProfiler. eYFP-SANS^{L195E} was significantly enriched in the nucleus compared to eYFP-SANS. White arrows in merge images: regions of interests (ROI) of fluorescence intensity plots; blue dashed lines: DAPI positive nuclear extension; black arrows: position of Z-projections. Scale bars: horizontal = 10 µm; vertical = 2 µm. Students t-test was performed for three independent experiments with a minimum of 75 cells.

 doi:10.20944/preprints202407.2436.v1

Unfortunately, we failed to design any synthetic mutant for SANS NES_3$^{406-420}$ since all genetic modifications introduced by site-specific mutagenesis in this region led to the emergence of a new NES in near proximity. Therefore, we decided to evaluate the role of SANS NES_3$^{406-420}$ in deletion constructs lacking the domains containing NES_3$^{406-420}$. The confirmed pathogenic frameshift variants of the human *USH1G* gene, SANS^{S278Pfs*71} and SANS^{S243*} (www.LOVD.nl/USH1G, accessed on 04th January 2023), which result in a premature stop at the end of CENTn2 or CENTc domain of SANS, respectively, fulfill this criterium (Figure 6A). Confocal microscopy of eYFP-tagged SANS^{S278Pfs*71} and SANS^{S243*} expressed in HeLa and HEK293T cells revealed enrichments of the pathogenic variants in the nucleus when compared to wild type SANS, as indicated by fluorescence intensity plotting and z-projection (Figure 6B, Figure S4A). CellProfiler-based quantifications confirmed the significant enrichment of both pathogenic variants in the nucleus compared to eYFP-SANS (Figure 6C, Figure S4B). The retention of SANS^{S278Pfs*71} and SANS^{S243*} in the nucleus indicates that NES_3$^{406-420}$ plays an additional pivotal role in SANS nuclear export.

In addition, we investigated the cellular localization of the frameshift mutation SANS^{V132Gfs*3}, which lacks almost the entire CENTn1 and all following C-terminal domains including all NLS and NES (Figure 6A). eYFP-tagged SANS^{V132Gfs*3} localized predominantly in the nucleus of HeLa and HEK293T cells, as indicated by fluorescence intensity plotting and z-projection (Figure 6B, Figure S4A). CellProfiler-based quantifications confirmed the significant enrichment of SANS^{V132Gfs*3} in the nucleus compared to eYFP-SANS (Figure 6C, Figure S4B).

Taken together our findings suggest that NES_1$^{181-195}$ and NES_3$^{406-420}$ but not NES_2$^{235-249}$ play a role in SANS nuclear export. Furthermore, present results on SANS pathogenic variants also suggest that alterations in nuclear shuttling may be part of the pathomechanisms leading to USH1G.

Preprints.org (www.preprints.org) | NOT PEER-REVIEWED | Posted: 30 July 2024 doi:10.20944/preprints202407.2436.v1

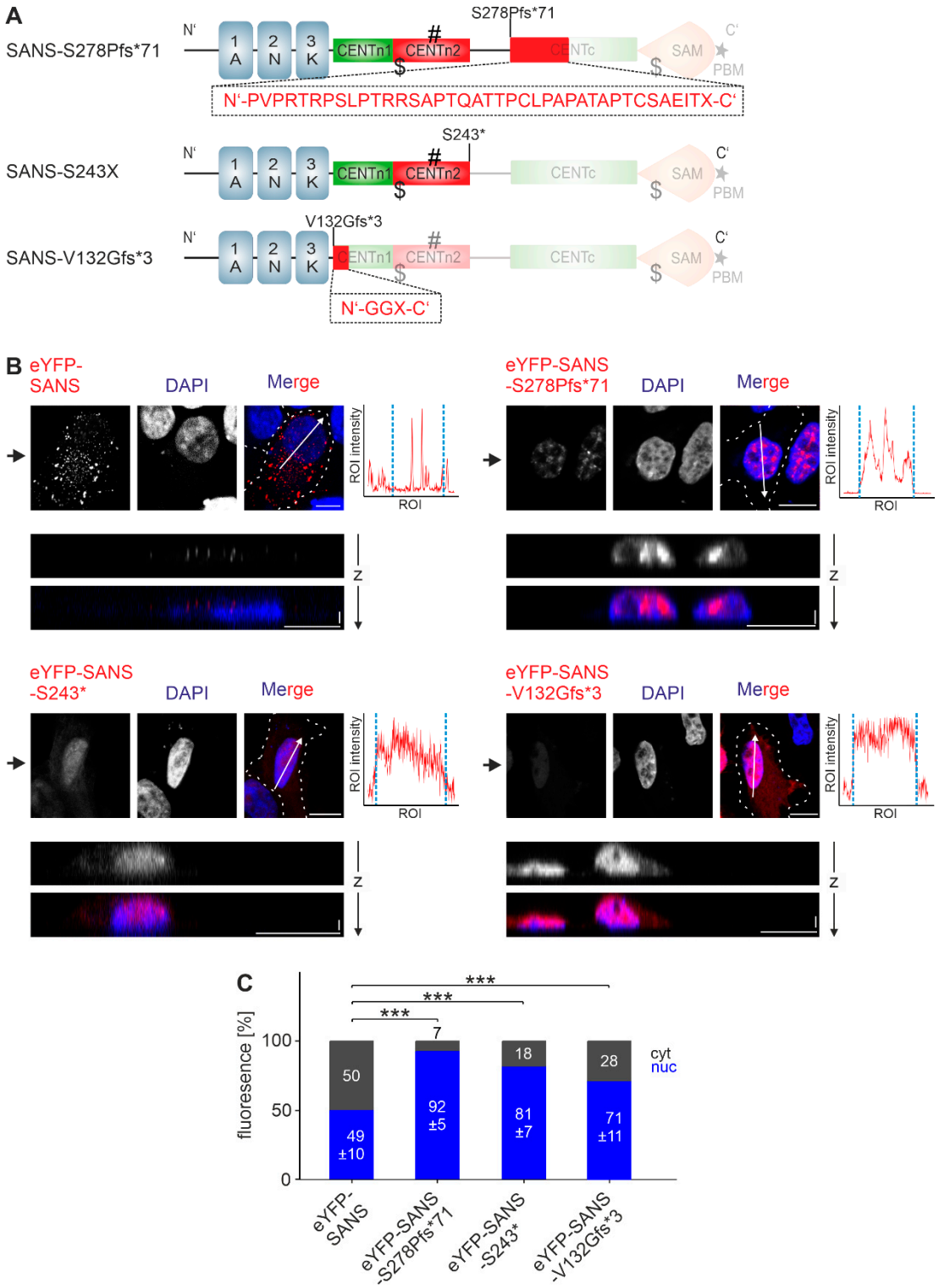

Figure 6. Localization of pathogenic variant of SANS in HeLa cells. (A) The pathogenic variant SANS^{S278Pfs*71} and SANS^{V132Gfs*3} are frameshift mutations which lead to missense extension (red boxes and amino acid sequences below) and a premature stop in CENTc or CENTn1, respectively. The pathogenic variant SANS^{S243*} has a premature stop codon after the CENTn2 domain. **(B)** Confocal microscopy of HeLa cells transfected with eYFP-SANS (red), eYFP-SANS^{S278Pfs*71}, eYFP-SANS^{S243*} and eYFP-SANS^{V132Gfs*3}, counterstained with DAPI. **(C)** Quantification of (B) with CellProfiler. All pathogenic variants were significantly enriched in the nucleus. White arrows in merge images: regions of interests (ROI) of fluorescence intensity plots; blue dashed lines: DAPI positive nuclear extension; black arrows: position of z-projections. Scale bars: horizontal = 10 µm; vertical = 2 µm. Students t-test was performed for three independent experiments with a minimum of 75 cells.

 doi:10.20944/preprints202407.2436.v1

3.6. SANS and Its Paralogue ANKS4B Are Localized to Different Subcellular Sites

SANS and its paralogue ANKS4B have nearly the same principal domain structure (Figure 1A), possess a homology of up to 80% in their amino acid sequences, and share common binding partners, such as USH1C/harmonin [5,14–16]. Since the differences in cellular function of closely related proteins often depend on the different spatial arrangements in the cell, we tested whether SANS and ANKS4B differ in their cytoplasmic/nuclear localization.

To determine the subcellular localization of ANKS4B we analyzed eYFP-tagged ANKS4B expressing HeLa cells (Figure 7A, B). Confocal microscopy showed that eYFP-ANKS4B was localized prominently in the cytoplasm, also indicated by fluorescence intensity plotting and z-projections. CellProfiler-based quantification demonstrated significantly lower nuclear localization of eYFP-ANKS4B compared to eYFP-SANS (Figure 7B).

NLStradamus predicted no NLS for ANKS4B. However, LocNES predicted six distinct NESs of various CRM1 binding motif classes for ANKS4B spanning its SAM-domain (Table 3) and predicted scores higher than 0.1, the threshold of LocNES [23].

Table 3. Predicted nuclear export sequences (NES) of ANKS4B.

NLS/NES	Sequence	Score	CRM1-class
NES_1$^{336\text{-}350}$	336-VEWEEDVVDATPLEV-350	0.191	1c
NES_2$^{338\text{-}352}$	338-WEEDVVDATPLEVFL-352	0.199	1c
NES_3$^{339\text{-}353}$	339-EEDVVDATPLEVFLL-353	0.205	1b
NES_4$^{346\text{-}360}$	346-TPLEVFLLSQHLEEF-360	0.181	2
NES_5$^{349\text{-}363}$	349-EVFLLSQHLEEFLPI-363	0.104	3
NES_6$^{362\text{-}376}$	362-PIFKREQIDLEALLL-376	0.251	2

To test whether these motifs are relevant for the subcellular localization we treated eYFP-ANKS4B transfected HeLa cells with the CRM1 inhibitor LMB (Figure 7C). CellProfiler-based quantification demonstrated that the LMB treatment resulted in a significant increase of eYFP-ANKS4B in the nucleus, which was not observed in DMSO treated control cells (Figure 7D).

Taken together, in contrast to SANS, the SANS paralogue ANKS4B is predominantly localized in the cytoplasm guaranteed by nuclear export based on CRM1 exportins.

 doi:10.20944/preprints202407.2436.v1

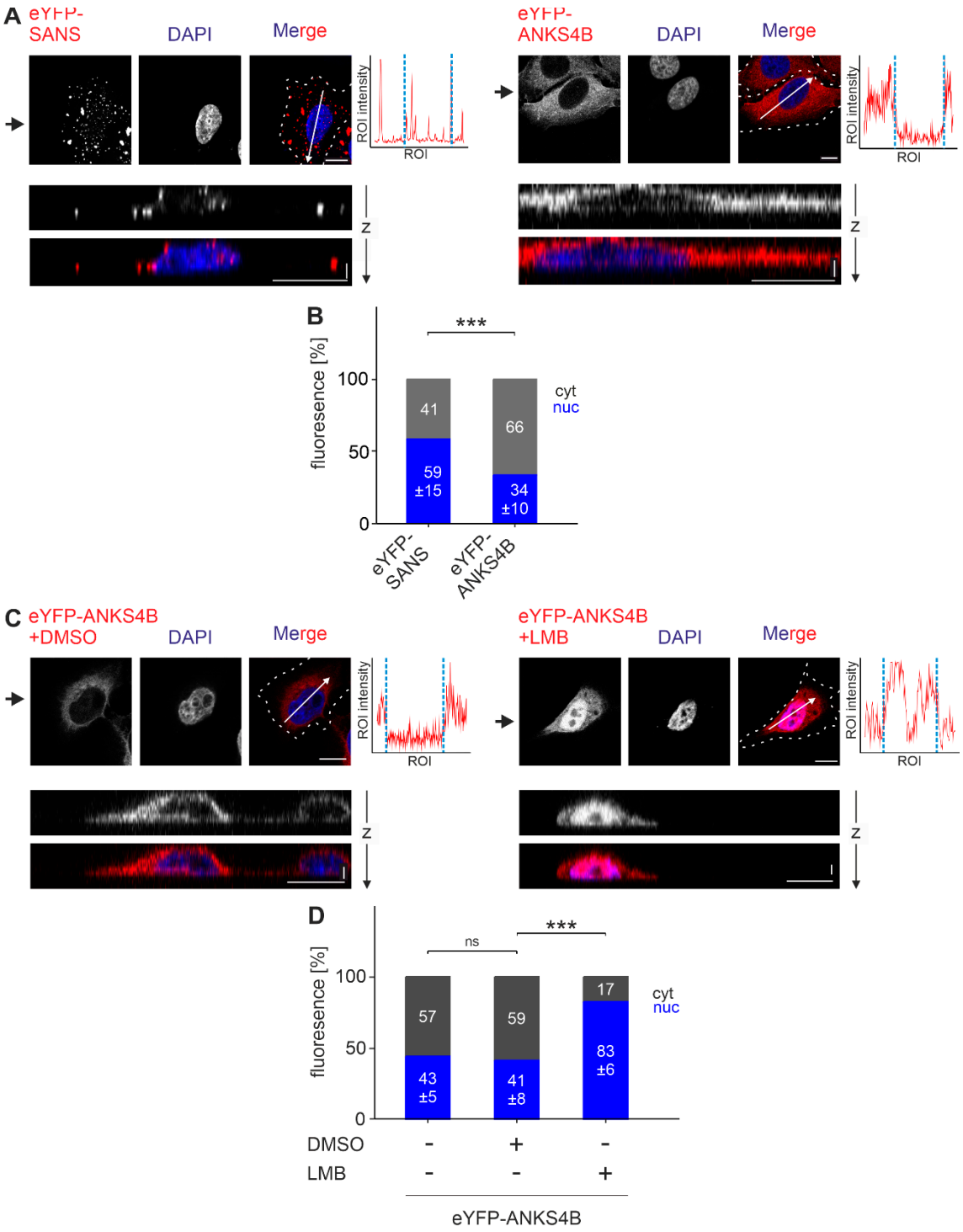

Figure 7. Comparison of the nuclear-cytoplasmic localization of SANS and its paralogue ANKS4B in HeLa cells. (A) Confocal microscopy of HeLa cells transfected with eYFP-SANS (red) or eYFP-ANKS4B (red), counterstained with DAPI. **(B)** Quantification of (A) with CellProfiler. eYFP-ANKS4B was highly enriched in the cytoplasm compared to eYFP-SANS. **(C)** Confocal microscopy of HeLa cells transfected with eYFP-ANKS4B (red), counterstained with DAPI. Cells were treated with DMSO or 5 nM CRM1 inhibitor Leptomycin-B (LMB). **(D)** Quantification of (C) with CellProfiler. eYFP-ANKS4B was highly enriched in the nucleus after treatment with LMB. White arrows in merge images: regions of interests (ROI) of fluorescence intensity plots; blue dashed lines: DAPI positive nuclear extension; black arrows: position of Z-projections. Scale bars: horizontal = 10 µm; vertical = 2 µm. Students t-test was performed for 3 independent experiments with a minimum of 75 cells.

 doi:10.20944/preprints202407.2436.v1

3.7. SANS and Its Paralog ANKS4B Differentially Interact with PRPF31

Next, we tested whether SANS and ANKS4B also differ in their binary interaction with the splicing molecule PRPF31 by fluorescence resonance energy transfer (FRET) acceptor photobleaching assays (Figure 8A, B) [4,32]. For this we co-transfected HeLa cells with eYFP-SANS or eYFP-ANKS4B, respectively, and eCFP-PRPF31. As controls, we used eYFP alone and harmonin-eCFP, which was previously shown to bind to ANKS4B and SANS [5,17]. FRET signals were normalized to 1 by the positive control eCFP-c-eYFP. The FRET pair eYFP-SANS-eCFP-PRPF31 generated significantly higher normalized FRET signals than the control pair eYFP-eCFP-PRPF31, confirming the binary binding of SANS and PRPF31 (Figure 8C) [4,12]. In contrast, the eYFP-ANKS4B-eCFP-PRPF31 FRET pair showed no increase in normalized FRET efficiencies when compared to the control eYFP-eCFP-PRPF31 pair. The height of the normalized FRET signals of eYFP-ANKS4B-harmonin-eCFP was in the range of the FRET signals of the FRET pair eYFP-SANS-eCFP-PRPF31 and significantly higher than the signals of the eYFP-eCFP-PRPF31 control pair, confirming the interaction of ANKS4B with harmonin as previously reported [17].

Next, we co-expressed eYFP-SANS or eYFP-ANKS4B with mRFP-PRPF31 or harmonin-mCherry, respectively in HeLa cells for subsequent confocal microscopy analyses (Figure 8C). Our analyses revealed that ANKS4B co-localized with harmonin in small droplets in the cytoplasm as observed before [14] but does not colocalize with PRPF31 in the nucleus which was strengthened by the negative Pearson coefficient (R = -0.14). In contrast, SANS co-localized with both harmonin and PRPF31, but in different compartments, namely in the cytoplasm and in the nucleus, respectively. Both co-localizations were supported by high positive Pearson coefficients (R = 0.96 and 0.92, respectively). The representative fluorescence intensity plots of tagged SANS and its interacting partners further demonstrated that SANS was almost completely found in the different compartments of its interacting partner. This finding indicated that SANS nuclear-cytoplasmic shuttling is additionally controlled by its interacting partners. However, further analyses with siRNA-based knockdown of PRPF31 showed no alteration of eYFP-SANS in HeLa cells (Figure S5).

In summary, our findings underscore the divergent nuclear localization/export sequences between SANS and ANKS4B paralog, resulting in differential subcellular localization patterns and cellular functions.

 doi:10.20944/preprints202407.2436.v1

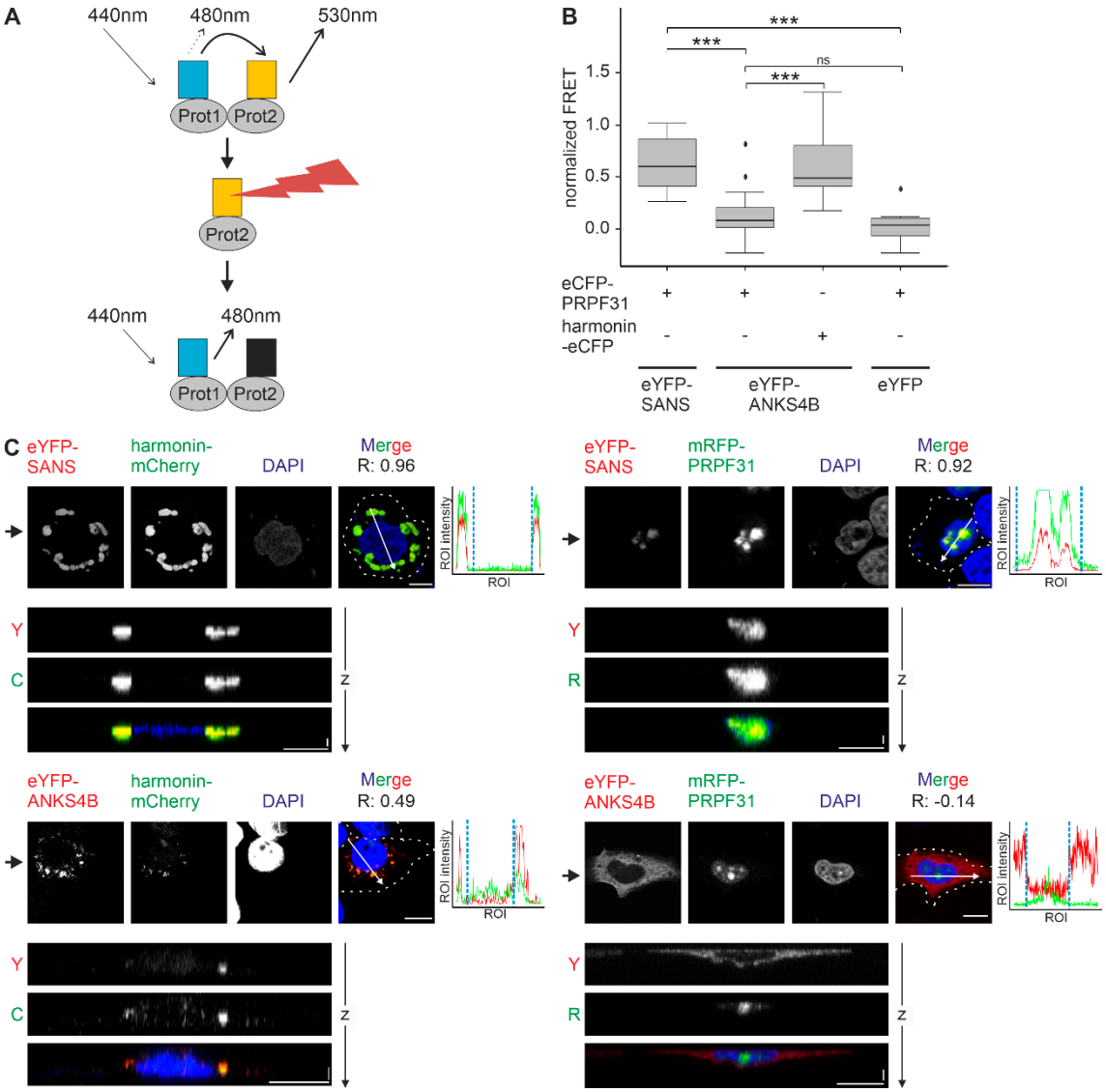

Figure 8. ANKS4B binary interaction in the nucleus. (A) Illustration of the FRET acceptor bleach assay. Interaction of two proteins tagged with either eCFP (blue) or eYFP (yellow) leads to FRET (upper). The acceptor (eYFP) is bleached (flash symbol) (middle), which leads to increased emission of the donor (eCFP) (lower). **(B)** FRET assay in co-transfected HeLa cells. FRET efficiencies were normalized to 1 by the fused eCFP-c-eYFP FRET pair (positive control). FRET pair eYFP-ANKS4B-eCFP-PRPF31 show not a significant increase in the normalized FRET efficiencies when compared to eYFP FRET pair negative controls. Outliers are shown as dots above/below the boxplots. Dunn's test after a Kruskal-Wallis test was performed for three independent experiments. **(C)** Confocal microscopy of HeLa cells co-transfected with eYFP-SANS (red) or eYFP-ANKS4B (red) and harmonin-mCherry (green) or mRFP-PRPF31 (green), counterstained with DAPI. eYFP-ANKS4B only co-localized with harmonin-mCherry but not with mRFP-PRPF31. White arrows in merge images: regions of interests (ROI) of fluorescence intensity plots; blue dashed lines: DAPI positive nuclear extension; black arrows: position of Z-projections. Scale bars: horizontal = 10 µm; vertical = 2 µm. Pearson coefficient R values indicate co-localization.

4. Discussion

The protein traffic across the nuclear pores is mostly mediated by members of karyopherin-β (or Kap) family commonly known as importins and exportins which specifically recognize NLSs and NESs of the cargo molecules [20]. In the present study, we provide several lines of evidence that the nuclear localization of SANS is regulated by an interplay of importins and exportins. We identified several importins and exportins in the previously described nuclear interactome of SANS

 doi:10.20944/preprints202407.2436.v1

[12]. *In silico* predictions revealed evolutionary conserved NLSs and NESs in the SANS sequences allowing the binding of importins and exportins. We experimentally confirmed the function of *in silico* predicted NLSs and NESs by quantifying the subcellular localization of SANS mutants *in situ*.

Multiple NLS and NES have been previously described for nuclear proteins, such as Fanconi anemia group A protein (FANCA) or enzyme 5-lipoxygenase (5-LO), respectively [33,34]. Our data on the two NLS suggests that NLS_1$^{213-224}$ localized in the central domain of SANS is the major NLS for the nuclear localization of SANS. In comparison to the N-terminal NLS_2$^{436-447}$, NLS_1$^{213-224}$ was scored higher in the predictions [23]. In addition, sequence alignments across vertebrates suggests that NLS_2$^{436-447}$ is less conserved. In NLS_2$^{436-447}$ charged amino acids are exchanged to uncharged in lower vertebrates probably affecting the interaction with importins. Importin binding is based on interactions with positively charged amino acids in NLSs of nuclear proteins [20] and exchanges to uncharged residues have been shown to alter NLS binding to importins [35]. In our study, we also experimentally induced such modifications by site-specific mutations of the NLSs in SANS. The quantitative data obtained showed that the decrease in nuclear localization of SANS with a mutated NLS_1$^{213-224}$ was highly significant in both HeLa and HEK293T cells. In contrast, mutated NLS_2$^{436-447}$ did not lead to a significant decrease in the nuclear localization of SANS in HeLa cells and only to a decrease of lower significance in HEK293T cells. Differences between cell lines in the nuclear-cytoplasmic partitioning of proteins were previously found to be related to differences in the metabolism between the cell lines [36–38].

Based on these data, we hypothesize that importins preferentially bind to NLS_1$^{213-224}$ of SANS for the import into the nucleus, e.g. to accomplish SANS' nuclear role in pre-mRNA splicing. Interestingly, NLS_1$^{213-224}$ is present in the central domain of SANS which represents the major binding site for numerous SANS interacting proteins [7,10,12]. Thus, the binding of cytoplasmic proteins such as myomegalin and whirlin to the central domain [7,10] is likely to compete with the binding of importins to the NLS_1$^{213-224}$. The competition in binding between importins and other cytoplasmic binding partners as a mechanism controlling the nuclear-cytoplasmic shuttling of nuclear proteins has been described previously [39,40]. Accordingly, the binding competition of cytoplasmic interaction partners of SANS and importins to the NLS sites could guarantee its cytoplasmic localization and thus ensure its cytoplasmic functions, e.g. in intracellular transport or ciliogenesis [7,9,11].

In addition, the binding of nuclear proteins may also facilitate nuclear import in a process known as "piggybacking" [41,42]. Since SANS was not completely removed from the nucleus when NLS_1$^{213-224}$ was mutated, and the overexpression of PRPF31 resulted in almost complete nuclear localization of co-expressed eYFP-SANS, we speculated that PRPF31 may play a piggyback role for SANS during nuclear import. However, since siRNA-mediated silencing of endogenous PRPF31 did not alter the nuclear-cytoplasmic shuttling of SANS we rejected this hypothesis. Alternatively, binding of importins to NLS_2$^{436-447}$ or binding of the identified importins, found in the SANS interactome, to non-classical NLS, which are not predictable by prediction tools may compensate for an absence of NLS_1$^{213-224}$.

Inhibition of the nuclear export by LMB suggests CRM1-dependent nuclear export of SANS. The analysis of the three predicted NES of SANS suggests NES_1$^{181-195}$ of the CENTn2 domain and NES_3$^{406-420}$ of the SAM domain as the major NES for the nuclear-cytoplasmic shuttling of SANS. All three predicted NESs are above the threshold for qualifying NESs and are highly conserved, except for NES_2$^{235-249}$, which differs in 3 of 5 vertebrates in the first residue. As expected for potent NESs, the site-specific mutations resulting in a non-functional NES_1$^{181-195}$ and the deletion variants of SANS lacking the NES_3$^{406-420}$ led to a highly significant increase of their nuclear localization in HeLa and HEK293T cells. In contrast, mutated NES_2$^{235-249}$ did not lead to a significant increase in its nuclear localization. Interestingly, NES_1$^{181-195}$ and NES_3$^{406-420}$ of SANS belong to different classes of CRM1 motifs that can differ in the binding affinity of CRM1 [43] and thereby, probably also in the nuclear export efficiency.

In comparison to SANS, its paralogue ANSK4B was far less abundant localized in the nucleus, which correlates with the lack of any known nuclear function of ANKS4B [14,17]. At first glance, the

 doi:10.20944/preprints202407.2436.v1

absence of ANKS4B might be caused because its sequence does not contain an NLS since none of the predicted tools applied, predicted a NLS for importin binding in ANKS4B, but several NESs suitable for CRM1 exportin binding. Interestingly, after inhibition of CRM1, more than 80% of the ANKS4B was located in the nucleus. This raises the question of how ANKS4B shuttles into the nucleus. In comparison to SANS (~51.5 kDa https://www.uniprot.org/uniprotkb/Q495M9/entry) ANKS4B (~46 kDa https://www.uniprot.org/uniprotkb/Q8N8V4/entry) is smaller, in the range of the size to diffuse passively through the nuclear pore complex commonly reported between 40 to 50 kDa [19]. However, we also found that the much larger eYFP-tagged ANKS4B ~75 kDa, which we monitored in our experiments, localized in the nucleus. The reason for this is possible that this size exclusion for free diffusion through the NPC is not as effective as assumed. Indeed, more recent findings indicate that larger macromolecules of > 100 kDa can also diffuse through the NPC [44]. Alternatively, as known for other proteins and already discussed above for SANS the nuclear import of ANKS4B may also be mediated by non-canonical NLS, which cannot be predicted by prediction tools [20,45]. Although we could not fully elucidate the regulation of ANKS4B import into the nucleus, our results confirm the previously shown predominantly cytoplasmic localization of ANKS4B. However, once ANKS4B enters the nucleus, it is immediately exported back into the cytoplasm mediated by the CRM1 exportin. This mechanism ensures that ANKS4B is available for its primary functions in the cytoplasm.

In our study, we provide evidence that nuclear-cytoplasmic shuttling of SANS and ANSK4B is coordinated by the selective binding of karyopherins to NLSs and NESs and determines their compartment-specific function. In the cell, protein functions and their regulations are commonly fine-tuned by post-translational modifications such as site-specific reversible phosphorylation [38,46,47]. Therefore, it is not surprising that reversible phosphorylation also emerges as an important process for regulating the nuclear availability of proteins [48]. Interestingly, we previously demonstrated that the kinase inhibitor D-ribofuranosylbenzimidazole (DRB) increases the abundance of SANS in the nucleus due to the inhibition of the phosphorylation at S422 (see Fig. S5 in [9]). S422 is a CK2 (casein kinase 2) phosphosite near NES_3$^{406-420}$. Therefore, it is tempting to speculate that CK2-mediated phosphorylation not only inhibits MAGI2 from binding to the internal PDZ-binding motif (PBM) in SANS-SAM [9] but may also regulate the binding of CRM1 to the NES.

While for the SANS encoding *USH1G* gene, more than 70 pathogenic variants have been identified thus far leading to deaf-blindness in patients [49] (www.LOVD.nl/USH1G) to our knowledge defects in ANKS4B have not been associated with a disease [18]. We have previously demonstrated that pathogenic variants of USH1G/SANS variants can lead to the disruption of fundamental cellular processes in both the cytoplasm and the nucleus: While USH1G/SANS variants lead to altered ciliogenesis and intracellular transport in the cytoplasm [10,11], they cause defects in pre-mRNA splicing in the nucleus [12]. Here we show that these SANS variants are highly enriched in the nucleus due to the defect in nuclear-cytoplasmic shuttling. Probably the lack of NESs leads to defects in nuclear export.

Although the SANS variants are targeted into the nucleus, they cannot fulfill their functions in the splicing process there, as we have previously demonstrated [12]. Possibly, not all interaction partners that interact with SANS during proper activation of the spliceosome can interact with the mutated, truncated versions of the scaffold protein. Probably more importantly, due to its pathogenic mutations, SANS is no longer available for its functions in the cytoplasm. A combination of defects in cytoplasmic trafficking and ciliogenesis as well as in pre-RNA splicing in the nucleus may underlie the pathology leading to USH1G. This complex scenario may be present in the retinal cells in the eye. In the inner ear, USH1G-associated deafness is more likely caused by defects in the assembly of mechanosensitive tip-link complex in the stereocilia of auditory hair cells [13].

5. Conclusions

USH1G/SANS is a multifunctional scaffold protein that participates in various cellular processes executed in different compartments of the cell, namely in the cytoplasm or nucleus. To fulfill its specific tasks, efficient and controlled nuclear-cytoplasmic shuttling of the SANS protein is mediated

by karyopherins binding to NLSs and NESs in the SANS. This is very different from its strict cytoplasmic paralogue ANKS4B, in which several NESs guarantee its localization and function in the cytoplasm. Finally, we provide evidence that the dysregulation and disruption of SANS´ nuclear-cytoplasmic shuttling can be relevant for the development of the USH disease in USH1G patients.

Supplementary Materials: The following supporting information can be downloaded at: Preprints.org. Supplementary_Figure_File.docx: all Figures S1-S5 referred to in this work; Table_S1.xlsx: GO-term analysis of SANS nuclear interactome from [12]; CellProfiler workflow available on GitHub: https://github.com/LabWolfrum/Fritze_et_al_2024_SANS_Nuclear_localization

Author Contributions: J.S.F. set up and carried out most of the experiments. F.F.S. carried out some cloning and experiments. J.S.F. and U.W. designed the studies and wrote the manuscript. All authors proofread the manuscript.

Funding: This study was supported by funds from the FAUN-Stiftung, Nuremberg, The Foundation Fighting Blindness (FFB) [PPA-0717-0719-RAD], and DFG (Project-No.: 521147274) to U.W..

Data Availability Statement: All raw data are available through contacting the corresponding author.

Acknowledgments: We thank Ronald Roepman (Human Genetics, Nijmegen) and Katja Luck (IMB, Mainz) for the contribution of several plasmids and constructs used in this study. We thank Christof Rickert (LMCF, JGU), the Microscopy Core Facility IMB, Mark Zorin (IMP, Mainz), Ulrike Maas (IMP, Mainz) and Joshua Linnert (IMP, Mainz) for their technical support. J.S.F. was enrolled in the International PhD Programme (IPP) Mainz.

Conflicts of Interest: The authors declare that the research was conducted in the absence of any commercial or financial relationships that could be construed as a potential conflict of interest.

References

1. Weil, D.; El-Amraoui, A.; Masmoudi, S.; Mustapha, M.; Kikkawa, Y.; Laine, S.; Delmaghani, S.; Adato, A.; Nadifi, S.; Zina, Z. Ben; et al. Usher Syndrome Type I G (USH1G) Is Caused by Mutations in the Gene Encoding SANS, a Protein That Associates with the USH1C Protein, Harmonin. *Hum Mol Genet* **2003**, *12*, 463–471, doi:10.1093/hmg/ddg051.
2. Fuster-Garcia, C.; Garcia-Bohorquez, B.; Rodriguez-Munoz, A.; Aller, E.; Jaijo, T.; Millan, J.M.; Garcia-Garcia, G. Usher Syndrome: Genetics of a Human Ciliopathy. *Int J Mol Sci* **2021**, *22*, doi:10.3390/ijms22136723.
3. Delmaghani, S.; El-Amraoui, A. The Genetic and Phenotypic Landscapes of Usher Syndrome: From Disease Mechanisms to a New Classification. *Hum Genet* **2022**, *141*, 709–735, doi:10.1007/S00439-022-02448-7.
4. Fritze, J.S.; Stiehler, F.F.; Wolfrum, U. Pathogenic Variants in USH1G/SANS Alter Protein Interaction with Pre-RNA Processing Factors PRPF6 and PRPF31 of the Spliceosome. *Int J Mol Sci* **2023**, *24*, doi:10.3390/IJMS242417608.
5. Adato, A.; Lefevre, G.; Delprat, B.; Michel, V.; Michalski, N.; Chardenoux, S.; Weil, D.; El-Amraoui, A.; Petit, C. Usherin, the Defective Protein in Usher Syndrome Type IIA, Is Likely to Be a Component of Interstereocilia Ankle Links in the Inner Ear Sensory Cells. *Hum Mol Genet* **2005**, *14*, 3921–3932, doi:10.1093/hmg/ddi416.
6. Maerker, T.; van Wijk, E.; Overlack, N.; Kersten, F.F.J.; Mcgee, J.; Goldmann, T.; Sehn, E.; Roepman, R.; Walsh, E.J.; Kremer, H.; et al. A Novel Usher Protein Network at the Periciliary Reloading Point between Molecular Transport Machineries in Vertebrate Photoreceptor Cells. *Hum Mol Genet* **2008**, *17*, 71–86, doi:10.1093/hmg/ddm285.
7. Overlack, N.; Kilic, D.; Bauss, K.; Marker, T.; Kremer, H.; van Wijk, E.; Wolfrum, U.; Bauß, K.; Märker, T.; Kremer, H.; et al. Direct Interaction of the Usher Syndrome 1G Protein SANS and Myomegalin in the Retina. *Biochim Biophys Acta* **2011**, *1813*, 1883–1892, doi:10.1016/j.bbamcr.2011.05.015.
8. Papal, S.; Cortese, M.; Legendre, K.; Sorusch, N.; Dragavon, J.; Sahly, I.; Shorte, S.; Wolfrum, U.; Petit, C.; El-Amraoui, A. The Giant Spectrin BetaV Couples the Molecular Motors to Phototransduction and Usher Syndrome Type I Proteins along Their Trafficking Route. *Hum Mol Genet* **2013**, *22*, 3773–3788, doi:10.1093/hmg/ddt228.
9. Bauss, K.; Knapp, B.; Jores, P.; Roepman, R.; Kremer, H.; Wijk, E. V; Marker, T.; Wolfrum, U. Phosphorylation of the Usher Syndrome 1G Protein SANS Controls Magi2-Mediated Endocytosis. *Hum Mol Genet* **2014**, *23*, 3923–3942, doi:10.1093/hmg/ddu104.

10. Sorusch, N.; Baub, K.; Plutniok, J.; Samanta, A.; Knapp, B.; Nagel-Wolfrum, K.; Wolfrum, U. Characterization of the Ternary Usher Syndrome SANS/Ush2a/Whirlin Protein Complex. *Hum Mol Genet* **2017**, *26*, 1157–1172, doi:10.1093/hmg/ddx027.
11. Sorusch, N.; Yildirim, A.; Knapp, B.; Janson, J.; Fleck, W.; Scharf, C.; Wolfrum, U. SANS (USH1G) Molecularly Links the Human Usher Syndrome Protein Network to the Intraflagellar Transport Module by Direct Binding to IFT-B Proteins. *Front Cell Dev Biol* **2019**, *7*, 216, doi:10.3389/fcell.2019.00216.
12. Yildirim, A.; Mozaffari-Jovin, S.; Wallisch, A.K.; Schäfer, J.; Ludwig, S.E.J.; Urlaub, H.; Lührmann, R.; Wolfrum, U. SANS (USH1G) Regulates Pre-MRNA Splicing by Mediating the Intra-Nuclear Transfer of Tri-SnRNP Complexes. *Nucleic Acids Res* **2021**, *49*, 5845–5866, doi:10.1093/nar/gkab386.
13. Caberlotto, E.; Michel, V.; Foucher, I.; Bahloul, A.; Goodyear, R.J.; Pepermans, E.; Michalski, N.; Perfettini, I.; Alegria-Prévot, O.; Chardenoux, S.; et al. Usher Type 1G Protein sans Is a Critical Component of the Tip-Link Complex, a Structure Controlling Actin Polymerization in Stereocilia. *Proc Natl Acad Sci U S A* **2011**, *108*, 5825–5830, doi:10.1073/pnas.1017114108.
14. He, Y.; Li, J.; Zhang, M. Myosin VII, USH1C, and ANKS4B or USH1G Together Form Condensed Molecular Assembly via Liquid-Liquid Phase Separation. *Cell Rep* **2019**, *29*, 974-986.e4, doi:10.1016/j.celrep.2019.09.027.
15. Yan, J.; Pan, L.; Chen, X.; Wu, L.; Zhang, M. The Structure of the Harmonin/sans Complex Reveals an Unexpected Interaction Mode of the Two Usher Syndrome Proteins. *Proc Natl Acad Sci U S A* **2010**, *107*, 4040–4045, doi:10.1073/pnas.0911385107.
16. Li, J.; He, Y.; Lu, Q.; Zhang, M. Mechanistic Basis of Organization of the Harmonin/USH1C-Mediated Brush Border Microvilli Tip-Link Complex. *Dev Cell* **2016**, *36*, 179–189, doi:10.1016/J.DEVCEL.2015.12.020.
17. Crawley, S.W.; Weck, M.L.; Grega-Larson, N.E.; Shifrin, D.A.; Tyska, M.J. ANKS4B Is Essential for Intermicrovillar Adhesion Complex Formation. *Dev Cell* **2016**, *36*, 190–200, doi:10.1016/J.DEVCEL.2015.12.022.
18. Graves, M.J.; Matoo, S.; Choi, M.S.; Storad, Z.A.; El Sheikh Idris, R.A.; Pickles, B.K.; Acharya, P.; Shinder, P.E.; Arvay, T.O.; Crawley, S.W. A Cryptic Sequence Targets the Adhesion Complex Scaffold ANKS4B to Apical Microvilli to Promote Enterocyte Brush Border Assembly. *J Biol Chem* **2020**, *295*, 12588–12604, doi:10.1074/JBC.RA120.013790.
19. Yang, Y.; Guo, L.; Chen, L.; Gong, B.; Jia, D.; Sun, Q. Nuclear Transport Proteins: Structure, Function, and Disease Relevance. *Signal Transduct Target Ther* **2023**, *8*, doi:10.1038/S41392-023-01649-4.
20. Wing, C.E.; Fung, H.Y.J.; Chook, Y.M. Karyopherin-Mediated Nucleocytoplasmic Transport. *Nat Rev Mol Cell Biol* **2022**, *23*, 307–328, doi:10.1038/S41580-021-00446-7.
21. Wiemann, S.; Pennacchio, C.; Hu, Y.; Hunter, P.; Harbers, M.; Amiet, A.; Bethel, G.; Busse, M.; Carninci, P.; Diekhans, M.; et al. The ORFeome Collaboration: A Genome-Scale Human ORF-Clone Resource. *Nat Methods* **2016**, *13*, 191–192, doi:10.1038/NMETH.3776.
22. Schindelin, J.; Rueden, C.T.; Hiner, M.C.; Eliceiri, K.W. The ImageJ Ecosystem: An Open Platform for Biomedical Image Analysis. *Mol Reprod Dev* **2015**, *82*, 518–529, doi:10.1002/mrd.22489.
23. Ba, A.N.N.; Pogoutse, A.; Provart, N.; Moses, A.M. NLStradamus: A Simple Hidden Markov Model for Nuclear Localization Signal Prediction. *BMC Bioinformatics* **2009**, *10*, doi:10.1186/1471-2105-10-202.
24. Xu, D.; Marquis, K.; Pei, J.; Fu, S.C.; Cağatay, T.; Grishin, N. V.; Chook, Y.M. LocNES: A Computational Tool for Locating Classical NESs in CRM1 Cargo Proteins. *Bioinformatics* **2015**, *31*, 1357–1365, doi:10.1093/bioinformatics/btu826.
25. Stirling, D.R.; Swain-Bowden, M.J.; Lucas, A.M.; Carpenter, A.E.; Cimini, B.A.; Goodman, A. CellProfiler 4: Improvements in Speed, Utility and Usability. *BMC Bioinformatics* **2021**, *22*, doi:10.1186/S12859-021-04344-9.
26. Positteam Download RStudio - Posit Available online: https://posit.co/downloads/ (accessed on 24 July 2023).
27. Zhou, Y.; Liu, F.; Xu, Q.; Yang, B.; Li, X.; Jiang, S.; Hu, L.; Zhang, X.; Zhu, L.; Li, Q.; et al. Inhibiting Importin 4-Mediated Nuclear Import of CEBPD Enhances Chemosensitivity by Repression of PRKDC-Driven DNA Damage Repair in Cervical Cancer. *Oncogene* **2020**, *39*, 5633–5648, doi:10.1038/S41388-020-1384-3.
28. Levin, A.; Neufeldt, C.J.; Pang, D.; Wilson, K.; Loewen-Dobler, D.; Joyce, M.A.; Wozniak, R.W.; Tyrrell, D.L.J. Functional Characterization of Nuclear Localization and Export Signals in Hepatitis C Virus Proteins and Their Role in the Membranous Web. *PLoS One* **2014**, *9*, doi:10.1371/JOURNAL.PONE.0114629.

29. Pemberton, L.F.; Paschal, B.M. Mechanisms of Receptor-Mediated Nuclear Import and Nuclear Export. *Traffic* **2005**, *6*, 187–198, doi:10.1111/J.1600-0854.2005.00270.X.
30. Shoubridge, C.; Tan, M.; Fullston, T.; Cloosterman, D.; Coman, D.; McGillivray, G.; Mancini, G.; Kleefstra, T.; Gécz, J. Mutations in the Nuclear Localization Sequence of the Aristaless Related Homeobox; Sequestration of Mutant ARX with IPO13 Disrupts Normal Subcellular Distribution of the Transcription Factor and Retards Cell Division. *Pathogenetics* **2010**, *3*, doi:10.1186/1755-8417-3-1.
31. Jans, D.A.; Martin, A.J.; Wagstaff, K.M. Inhibitors of Nuclear Transport. *Curr Opin Cell Biol* **2019**, *58*, 50–60, doi:10.1016/J.CEB.2019.01.001.
32. Karpova, T.S.; Baumann, C.T.; He, L.; Wu, X.; Grammer, A.; Lipsky, P.; Hager, G.L.; McNally, J.G. Fluorescence Resonance Energy Transfer from Cyan to Yellow Fluorescent Protein Detected by Acceptor Photobleaching Using Confocal Microscopy and a Single Laser. *J Microsc* **2003**, *209*, 56–70, doi:10.1046/j.1365-2818.2003.01100.x.
33. Lou, M.; Pang, C.W.M.; Gerken, A.E.; Brock, T.G. Multiple Nuclear Localization Sequences Allow Modulation of 5-Lipoxygenase Nuclear Import. *Traffic* **2004**, *5*, 847–854, doi:10.1111/J.1600-0854.2004.00227.X.
34. Ferrer, M.; Rodríguez, J.A.; Spierings, E.A.; de Winter, J.P.; Giaccone, G.; Kruyt, F.A.E. Identification of Multiple Nuclear Export Sequences in Fanconi Anemia Group A Protein That Contribute to CRM1-Dependent Nuclear Export. *Hum Mol Genet* **2005**, *14*, 1271–1281, doi:10.1093/HMG/DDI138.
35. Smith, K.M.; Di Antonio, V.; Bellucci, L.; Thomas, D.R.; Caporuscio, F.; Ciccarese, F.; Ghassabian, H.; Wagstaff, K.M.; Forwood, J.K.; Jans, D.A.; et al. Contribution of the Residue at Position 4 within Classical Nuclear Localization Signals to Modulating Interaction with Importins and Nuclear Targeting. *Biochim Biophys Acta Mol Cell Res* **2018**, *1865*, 1114–1129, doi:10.1016/J.BBAMCR.2018.05.006.
36. De Ganck, A.; Hubert, T.; Van Impe, K.; Geelen, D.; Vandekerckhove, J.; De Corte, V.; Gettemans, J. A Monopartite Nuclear Localization Sequence Regulates Nuclear Targeting of the Actin Binding Protein Myopodin. *FEBS Lett* **2005**, *579*, 6673–6680, doi:10.1016/J.FEBSLET.2005.10.054.
37. Kopp, M.; Rotan, O.; Papadopoulos, C.; Schulze, N.; Meyer, H.; Epple, M. Delivery of the Autofluorescent Protein R-Phycoerythrin by Calcium Phosphate Nanoparticles into Four Different Eukaryotic Cell Lines (HeLa, HEK293T, MG-63, MC3T3): Highly Efficient, but Leading to Endolysosomal Proteolysis in HeLa and MC3T3 Cells. *PLoS One* **2017**, *12*, doi:10.1371/JOURNAL.PONE.0178260.
38. Napolitano, G.; Esposito, A.; Choi, H.; Matarese, M.; Benedetti, V.; Di Malta, C.; Monfregola, J.; Medina, D.L.; Lippincott-Schwartz, J.; Ballabio, A. MTOR-Dependent Phosphorylation Controls TFEB Nuclear Export. *Nat Commun* **2018**, *9*, doi:10.1038/s41467-018-05862-6.
39. Kumagai, A.; Dunphy, W.G. Binding of 14-3-3 Proteins and Nuclear Export Control the Intracellular Localization of the Mitotic Inducer Cdc25. *Genes Dev* **1999**, *13*, 1067–1072, doi:10.1101/GAD.13.9.1067.
40. Eberhard, D.A.; Karns, L.R.; VandenBerg, S.R.; Creutz, C.E. Control of the Nuclear-Cytoplasmic Partitioning of Annexin II by a Nuclear Export Signal and by P11 Binding. *J Cell Sci* **2001**, *114*, 3155–3166, doi:10.1242/JCS.114.17.3155.
41. Macara, I.G. Transport into and out of the Nucleus. *Microbiol Mol Biol Rev* **2001**, *65*, 570–594, doi:10.1128/MMBR.65.4.570-594.2001.
42. Tessier, T.M.; Macneil, K.M.; Mymryk, J.S. Piggybacking on Classical Import and Other Non-Classical Mechanisms of Nuclear Import Appear Highly Prevalent within the Human Proteome. *Biology (Basel)* **2020**, *9*, 1–20, doi:10.3390/BIOLOGY9080188.
43. Fung, H.Y.J.; Fu, S.C.; Chook, Y.M. Nuclear Export Receptor CRM1 Recognizes Diverse Conformations in Nuclear Export Signals. *Elife* **2017**, *6*, doi:10.7554/ELIFE.23961.
44. Timney, B.L.; Raveh, B.; Mironska, R.; Trivedi, J.M.; Kim, S.J.; Russel, D.; Wente, S.R.; Sali, A.; Rout, M.P. Simple Rules for Passive Diffusion through the Nuclear Pore Complex. *J Cell Biol* **2016**, *215*, doi:10.1083/JCB.201601004.
45. Bourgeois, B.; Hutten, S.; Gottschalk, B.; Hofweber, M.; Richter, G.; Sternat, J.; Abou-Ajram, C.; Göbl, C.; Leitinger, G.; Graier, W.F.; et al. Nonclassical Nuclear Localization Signals Mediate Nuclear Import of CIRBP. *Proc Natl Acad Sci U S A* **2020**, *117*, 8503–8514, doi:10.1073/PNAS.1918944117/-/DCSUPPLEMENTAL.
46. Sakiyama, H.; Wynn, R.M.; Lee, W.R.; Fukasawa, M.; Mizuguchi, H.; Gardner, K.H.; Repa, J.J.; Uyeda, K. Regulation of Nuclear Import/Export of Carbohydrate Response Element-Binding Protein (ChREBP):

Interaction of Anα-Helix of ChREBP with the 14-3-3 Proteins and Regulation by Phosphorylation. *Journal of Biological Chemistry* **2008**, *283*, 24899–24908, doi:10.1074/jbc.M804308200.

47. Wang, L.; Liu, X.; Gusev, E.; Wang, C.; Fagotto, F. Regulation of the Phosphorylation and Nuclear Import and Export of β-Catenin by APC and Its Cancer-Related Truncated Form. *J Cell Sci* **2014**, *127*, 1647–1659, doi:10.1242/jcs.131045.
48. Nardozzi, J.D.; Lott, K.; Cingolani, G. Phosphorylation Meets Nuclear Import: A Review. *Cell Commun Signal* **2010**, *8*, doi:10.1186/1478-811X-8-32.
49. Fokkema, I.F.A.C.; Taschner, P.E.M.; Schaafsma, G.C.P.; Celli, J.; Laros, J.F.J.; den Dunnen, J.T. LOVD v.2.0: The next Generation in Gene Variant Databases. *Hum Mutat* **2011**, *32*, 557–563, doi:10.1002/humu.21438.